A novel, SiPM-array-based, monolithic scintillator detector for PET



2009 Phys. Med. Biol. 54 3501

(http://iopscience.iop.org/0031-9155/54/11/015)

Phys. Med. Biol. **54** (2009) 3501–3512 doi:10.1088/0031-9155/54/11/015

# A novel, SiPM-array-based, monolithic scintillator detector for PET

**Dennis R Schaart[1], Herman T van Dam[1], Stefan Seifert[1], Ruud Vinke[2], Peter Dendooven[2], Herbert Löhner[2] and Freek J Beekman[1,3]**

[1] Delft University of Technology, Radiation Detection & Medical Imaging, Mekelweg 15, 2629 JB Delft, The Netherlands
[2] Kernfysisch Versneller Instituut, University of Groningen, Zernikelaan 25, 9747 AA, Groningen, The Netherlands
[3] Image Sciences Institute, University Medical Centre Utrecht, Heidelberglaan 100, 3584 CG, Utrecht, The Netherlands

E-mail: d.r.schaart@tudelft.nl

Received 14 January 2009, in final form 24 March 2009
Published 15 May 2009
Online at stacks.iop.org/PMB/54/3501

**Abstract**

Silicon photomultipliers (SiPMs) are of great interest to positron emission tomography (PET), as they enable new detector geometries, for e.g., depth-of-interaction (DOI) determination, are MR compatible, and offer faster response and higher gain than other solid-state photosensors such as avalanche photodiodes. Here we present a novel detector design with DOI correction, in which a position-sensitive SiPM array is used to read out a monolithic scintillator. Initial characterization of a prototype detector consisting of a $4 \times 4$ SiPM array coupled to either the front or back surface of a 13.2 mm $\times$ 13.2 mm $\times$ 10 mm LYSO:$Ce^{3+}$ crystal shows that front-side readout results in significantly better performance than conventional back-side readout. Spatial resolutions $<$1.6 mm full-width-at-half-maximum (FWHM) were measured at the detector centre in response to an $\sim$0.54 mm FWHM diameter test beam. Hardly any resolution losses were observed at angles of incidence up to 45°, demonstrating excellent DOI correction. About 14% FWHM energy resolution was obtained. The timing resolution, measured in coincidence with a $BaF_2$ detector, equals 960 ps FWHM.

(Some figures in this article are in colour only in the electronic version)

## 1. Introduction

Positron emission tomography (PET) enables imaging of biological processes and is increasingly being used in the clinic as well as in biomedical research (Gambhir 2002, Nestle *et al* 2009, Phelps 2000, Rohren *et al* 2004). PET has proven its value in the diagnosing,

  

staging and restaging of cancer. It furthermore plays a growing role, e.g. in radiotherapy treatment planning, in radionuclide and chemotherapy monitoring and in other fields such as neurology and cardiology.

PET instrumentation is continuously being improved, driven by the need for better image quality and shorter scanning times. At the detector level, this requires higher spatial resolution—including correction for depth-of-interaction (DOI) errors, higher sensitivity, improved count-rate performance and better energy resolution (Lewellen 2008). In addition, clinical PET will benefit from further improvement of time-of-flight (TOF) performance (Moses 2007, Muehllehner and Karp 2006), as TOF-PET with ~600 ps coincidence resolving time (CRT) has already demonstrated significant improvement in image quality, especially in heavier patients (Surti *et al* 2007).

It is furthermore desirable to integrate complementary imaging modalities (Cherry 2004, Townsend 2008). For example, the combination of the functional and anatomical imaging capabilities of PET and x-ray CT, respectively, into hybrid PET/CT systems has had tremendous impact within the field of oncology (Beyer *et al* 2000, Czernin *et al* 2007, Israel and Kuten 2007). At present, various groups are working on the more difficult challenge of combining PET and MRI (Catana *et al* 2006, Judenhofer *et al* 2008, Shao *et al* 1997, Townsend 2008). Potential advantages of PET/MRI include the far better soft-tissue contrast of MRI compared to CT and the elimination of the CT dose, which tends to be responsible for most of the overall dose received by the patient during a PET/CT scan. True PET/MRI integration, however, requires PET detectors that are very compact, do not distort the operation of the MRI system and are insensitive to magnetic fields.

The ideal PET detector would perform optimally with respect to each of the above criteria and be affordable at the same time. Scintillation detectors based on solid-state photosensors are very promising in this respect. In contrast with conventional photomultiplier tubes (PMTs), such sensors can be made MR compatible. Furthermore, their small size enables novel detector geometries that allow DOI determination as well as a high detector packing fraction to maximize PET system sensitivity. The importance of sensitivity should not be underestimated as the reconstructed resolution of clinical PET images is often limited by the number of acquired counts rather than by the system resolution (Muehllehner and Karp 2006). Furthermore, combating the inherent physical limits on PET spatial resolution by compensating for positron range and non-collinearity in the image reconstruction process requires sufficient statistical quality of the acquired data (Cherry 2004).

Whereas solid-state photosensors such as PIN diodes and avalanche photodiodes (APDs) have been explored by many authors, a particularly interesting new class of devices is silicon photomultipliers (SiPMs) (Antich *et al* 1997, Bondarenko *et al* 2000, Britvitch *et al* 2007, Golovin and Saveliev 2004, Herbert *et al* 2007, McElroy *et al* 2007, Musienko *et al* 2007, Renker 2007). These can be fabricated using CMOS technology, offering the possibility of low cost when produced in large quantities. They have gains in the order of $\sim 10^6$ and are very fast, which is crucial for TOF-PET. In fact, CRTs of 237 ps full-width-at-half-maximum (FWHM) and 240 ps FWHM have recently been demonstrated using 3 mm × 3 mm SiPMs coupled to small crystals of, respectively, $LaBr_3:Ce^{3+}$ (Schaart *et al* 2008a) and $LYSO:Ce^{3+}$ (Kim *et al* 2008). As of very recently, SiPMs can be manufactured into compact arrays that can be used as position-sensitive light sensors in PET detectors (España *et al* 2008, Kolb *et al* 2008, Llosá *et al* 2008, Schaart *et al* 2008b).

The aim of this paper is to present an initial characterization of the first SiPM-array-based PET detector following the monolithic scintillator concept explored using APD arrays by Maas *et al* (2006, 2009). This monolithic approach has previously been shown to allow not only high resolution and excellent DOI correction but also very high system sensitivity

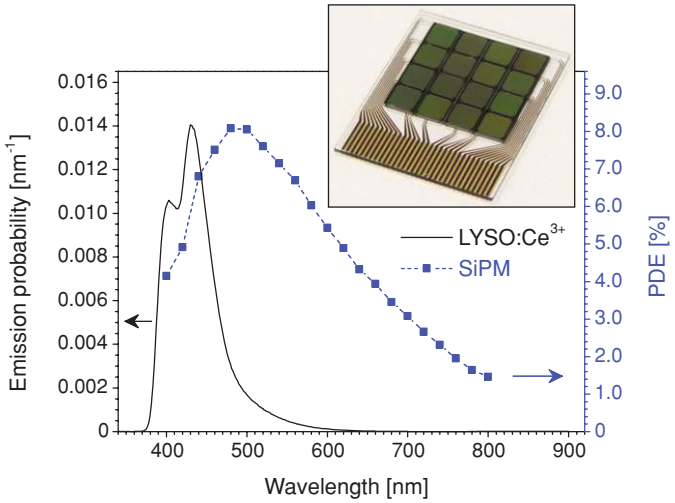


**Figure 1.** Photo-detection efficiency of the 2.85 mm × 2.85 mm active area of a single SiPM pixel of a SensL SPMArray 3035G16 at 2 V above the breakdown voltage (blue squares, right-hand *y*-axis), in comparison to the emission probability per nm per scintillation photon of a 3 mm × 3 mm × 3 mm LYSO:Ce$^{3+}$ crystal (solid black line, left-hand *y*-axis). The inset shows the essential parts of the SiPM array: 4 × 4 SiPM pixels mounted onto a glass substrate with readout tracks. Photograph courtesy SensL, Ireland.

(van der Laan *et al* 2007). Two readout geometries are compared in this work: front-side readout (FSR) and conventional back-side readout (BSR).

## 2. Materials and methods

### *2.1. Detector*

The detector prototype is based on a 13.2 mm × 13.2 mm × 10 mm monolithic LYSO:Ce$^{3+}$ scintillator with optically polished surfaces (Crystal Photonics). The 13.2 mm × 13.2 mm crystal surfaces match the sensitive area of the SiPM array, which is optically coupled to the crystal using the Sylgard 527 dielectric gel. All other faces of the crystal are covered with a highly reflective PTFE-based material (Spectralon). The SiPM array (SensL SPMArray 3035G16) is a 4 × 4 array of SiPM pixels mounted onto a 550 $\mu$m thick white float glass substrate using flip chip technology, see the inset in figure 1. The 16 silicon dies are mounted at a pitch of 3.3 mm. Each pixel has an active area of 2.85 mm × 2.85 mm, made up of 3640 Geiger-mode avalanche photodiodes (microcells). The SiPM array was operated at the manufacturer-specified bias voltage of 29.3 V, exceeding the breakdown voltage by 2.0 V corresponding to a gain of $\sim 10^6$.

The blue squares in figure 1 show the photo-detection efficiency (PDE) in air of the 2.85 mm × 2.85 mm active area of a single SiPM pixel at 2 V above breakdown (SensL, private communication). It is emphasized that these values are free of any contributions from after pulsing or crosstalk (SensL 2007). The solid black line in figure 1 shows the emission spectrum of a 3 mm × 3 mm × 3 mm LYSO:Ce$^{3+}$ crystal (Crystal Photonics), measured as described by De Haas and Dorenbos (2008). The effective PDE of the SiPM active area, weighted by the normalized LYSO:Ce$^{3+}$ emission spectrum, equals ∼5.9%. As the fractional active area of the array equals ∼75%, the effective PDE of the entire array in air is estimated to be ∼4.4%.

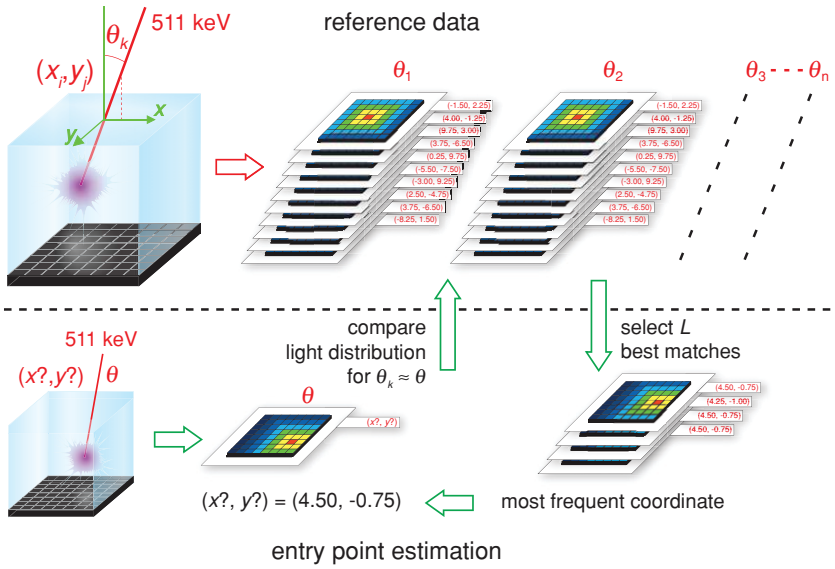


**Figure 2.** Schematic representation of the nearest-neighbour algorithm used to estimate the entry point ($x$, $y$) of the annihilation photon on the front surface of the crystal from the scintillation light distribution measured by the position-sensitive SiPM array. See the text for details.

### 2.2. *Position estimation*

Rather than the interaction point of the annihilation photon, its entry point on the crystal front surface is estimated, using the statistical algorithm described by Maas *et al* (2009). For convenience, we briefly summarize the method here. As indicated in figure 2, reference data are first collected by irradiating the detector with 511 keV photons at a series of known positions ($x_i$, $y_j$) and angles of incidence $\theta_k$ on the crystal front surface. At each position and angle, the light distributions of $n_{\mathrm{ref}}$ reference events are recorded. The entry point of an unknown annihilation photon is subsequently estimated by calculating the sum-of-squared-differences of its light distribution with those of all events in the reference set recorded at the $\theta_k$ closest to the angle of incidence $\theta$ of the unknown event. In a PET scanner, $\theta$ can be estimated from the positions of the two detectors triggering in coincidence (Maas *et al* 2009). A subset of the reference data consisting of $L$ closest matches (nearest neighbours) is selected, and the most frequently occurring entry point within this subset is assigned to the unknown event.

### 2.3. *Measurements*

Measurements were performed using the setup described by Maas *et al* (2009). Briefly, the detector is contained in a temperature-controlled box and can be irradiated at different positions and angles of incidence with a $<$1 mm diameter test beam of annihilation photons, defined by placing the detector close to a 0.5 mm diameter $^{22}$Na source and operating it in coincidence with a collimated BGO detector placed on the opposite side of the source. The SiPM signals were preamplified using a 16-channel readout board designed to minimize nonlinearity due to SiPM impedance variations. The design and characteristics of these preamplifiers have been described by Seifert *et al* (2008). The preamplified SiPM pulses were shaped and their

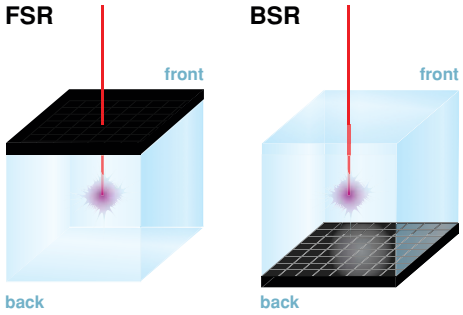


**Figure 3.** Schematic representation of the readout geometries investigated. Left: front-side readout (FSR) geometry. Right: back-side readout (BSR) geometry.

pulse heights digitized using the multichannel data acquisition system described by Maas *et al* (2009). In parallel, a trigger signal was generated by adding the 16 SiPM signals by means of a fast summing amplifier on the preamplifier board.

Spatial resolution measurements were performed by recording reference events at a rectangular, equidistant grid of reference beam positions $(x_i, y_j)$, having a pitch of 0.25 mm and covering the entire front surface of the crystal. At non-perpendicular incidence, the same reference grid was used and the lateral crystal surface that turned towards the beam was included in the measurement. The reference events were also used as test events, using the leave-one-out method described by Maas *et al* (2009). All measurements were conducted at ∼24 °C.

Pulse height spectra were derived by correcting the digitized pulse heights of all detector channels for offsets, adding the 16 corrected pulse heights of each event and normalizing the result such that the centre of the full-energy peak corresponded to 511 keV.

The detector timing resolution was determined by placing the detector in coincidence with a $BaF_2$ crystal on an XP2020Q PMT connected to an Ortec 579 fast filter amplifier (FFA) and an Ortec 935 constant fraction discriminator (CFD). The SiPM sum signal was fed into a second identical FFA and a LeCroy WavePro 7300 oscilloscope was used to measure the time difference between the CFD logic pulse and the moment at which the second FFA output signal crossed a fixed threshold corresponding to ∼10 keV. Only full-energy events were accepted.

## 3. Results

Measurements were performed in two different readout geometries: front-side readout (FSR), in which the SiPM array is placed on the crystal surface facing the radiation source, and conventional back-side readout (BSR), see figure 3. It is emphasized that FSR is possible without significantly disturbing the annihilation photon beam since the SiPM array is very thin and consists of low-$Z$ materials only. Specifically, a Monte Carlo simulation of the detector using GATE (Jan *et al* 2004) showed that the probability of a 511 keV photon undergoing at least one Compton or Raleigh interaction in the SiPM array before being detected (i.e. before undergoing at least one Compton and/or photoelectric interaction in the crystal) equals ∼3%.

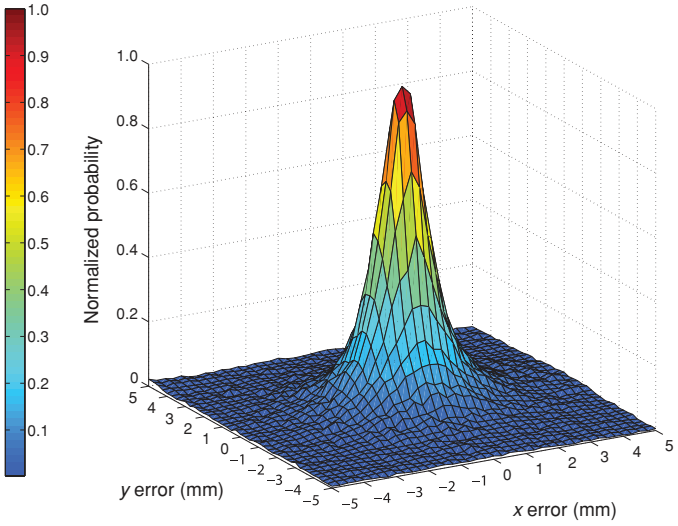


**Figure 4.** Detector spatial response to an ∼0.54 mm FWHM diameter test beam, measured in FSR geometry at the detector centre and at normal incidence using $n_{\mathrm{ref}} = 1000$ and $L = 750$.

**Table 1.** FWHM and FWTM of the spatial response at the detector centre at normal incidence. Results were obtained in FSR geometry and are not corrected for the ∼0.54 mm FWHM diameter test beam.

| Direction | FWHM (mm) | FWTM (mm) |
|---|---|---|
| *x* | 1.58 | 4.06 |
| *y* | 1.56 | 4.23 |

### *3.1. Spatial resolution*

The detector spatial response (i.e. the two-dimensional histogram of the differences between the true and estimated annihilation photon entry points) can in principle be derived at each point of the measurement grid. However, the number of events $n_{\mathrm{ref}}$ recorded at each point is limited, resulting in considerable statistical fluctuations if the histogram is determined for one such point only. As the spatial response appears to be approximately constant over the central area of the detector, the results obtained within the central 3.25 mm × 3.25 mm were combined into a single error histogram.

Figure 4 shows the corresponding result obtained in FSR geometry. The full-width-at-half-maximum (FWHM) and the full-width-at-tenth-maximum (FWTM) are shown in table 1. It is noted that these results still contain the influence of the ∼0.54 mm FWHM diameter test beam. Furthermore, they were obtained at a low-energy threshold of ∼50 keV applied to the sum of the 16 SiPM signals.

Interestingly, increasing the energy threshold to ∼400 keV hardly appears to improve these results (<1%). On first sight one might expect that low-energy events would be positioned less accurately due to the lower amount of scintillation light emitted. However, in most of these events the scintillation light will be emitted from a single (Compton) interaction location. In contrast, many of the events in the full-energy peak appear to involve multiple interactions within the crystal (see section 3.4). Events in which the scintillation light is emitted from

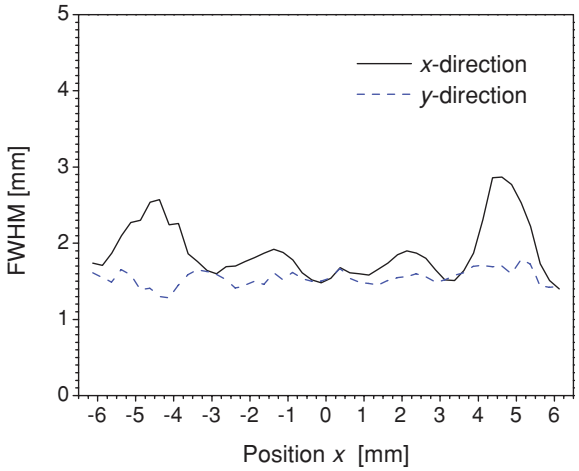


**Figure 5.** FWHM of the detector spatial response in the $x$-direction (solid black curve) and in the $y$-direction (dashed blue curve), as a function of $x$. Data were measured in FSR geometry at perpendicular incidence, using an ∼0.54 mm FWHM diameter test beam and with $n_{\text{ref}} = 1000$ and $L = 750$.

multiple interaction locations may be more difficult to position than single-interaction events. Apparently, the resulting average positioning accuracy is similar for events in the full-energy peak, most of which involve multiple interactions, and events in the Compton ridge, most of which involve a single interaction, so that the detector spatial resolution becomes almost independent of the energy threshold.

Similar to what was found in APD-based monolithic detectors by Maas *et al* (2009), the spatial resolution shows some degradation near the detector edges. For example, the solid black line in figure 5 shows the FWHM of the detector spatial response in the $x$-direction as a function of $x$. At each $x$, all results obtained between $x - 0.5$ mm and $x + 0.5$ mm (i.e. over the entire length of the crystal in the $y$-direction) were combined into a 2D error histogram in order to minimize statistical fluctuations. At ∼3 mm from the crystal edge, the FWHM starts to increase, until it reaches a maximum at ∼2 mm from the edge. At smaller distances the FWHM decreases again, as the error histograms are being truncated on one side by the crystal edge.

The dashed blue line in figure 5 shows the FWHM of the detector spatial response in the $y$-direction as a function of $x$, derived from the same error histograms used to obtain the solid black curve. Interestingly, no significant dependence of the FWHM in the $y$-direction on $x$ is observed. Conversely, the FWHM in the $y$-direction is found to depend on $y$, whereas the FWHM in the $x$-direction does not. Hence, the FWHM in a given direction ($x$ or $y$) is only affected by a crystal edge perpendicular to that direction, in agreement with what was found by Maas *et al* (2009).

### *3.2. FSR versus BSR*

In a further series of measurements, the resolutions obtained in different readout geometries and at different angles of incidence were compared. In these measurements, the $^{22}$Na point source had to be placed at a larger distance from the detector box to allow it to rotate. This resulted in a larger, but constant, test beam diameter of ∼0.64 mm FWHM.

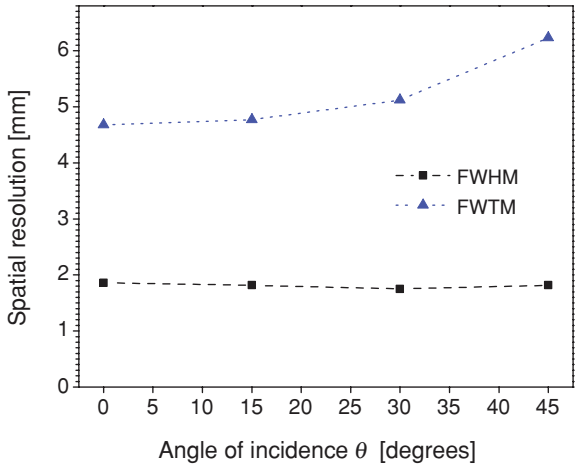


**Figure 6.** FWHM and FWTM of the average detector spatial response in the *x*-direction, measured as a function of the angle of incidence $\theta$ using an ∼0.64 mm FWHM diameter test beam. Data were obtained in FSR geometry with $n_{\text{ref}} = 250$ and $L = 1000$.

**Table 2.** Comparison of front- and back-side readout. Values represent the FWHM and FWTM in the *x*-direction of the detector spatial response at normal incidence, averaged over the entire detector surface, not corrected for the ∼0.64 mm FWHM diameter test beam.

| Readout geometry | FWHM (mm) | FWTM (mm) |
|---|---|---|
| Front-side readout (FSR) | 1.86 | 4.68 |
| Back-side readout (BSR) | 2.21 | 5.33 |

The results were analysed by combining the data obtained over the entire crystal surface into a single error histogram, which we will denote as the 'average detector spatial response'. It is noted that these results cannot be compared directly to those obtained at the detector centre (i.e. table 1 and figure 4), both because of the larger beam diameter and because of the larger FWHM values observed near the detector edges (see figure 5).

The FSR and BSR results are compared in table 2. FSR appears to perform considerably better than BSR. We therefore focus on FSR in the remainder of this work.

### *3.3. DOI correction*

Estimating the annihilation photon entry point has the advantage that DOI errors are, in principle, eliminated (Maas *et al* 2009). This intrinsic DOI correction was tested by irradiating the detector at different angles of incidence $\theta$ and deriving the average spatial response projected onto a plane perpendicular to the test beam. In this way, the results correlate directly with the uncertainty in the position of the line-of-response (LOR) in a PET scanner.

Figure 6 shows the FWHM and FWTM of the average detector response as a function of $\theta$, determined in FSR geometry using the same test beam diameter as in table 2. Hardly any spatial resolution losses are observed for angles of incidence of up to 45°. Only the FWTM increases slightly with increasing angle of incidence.

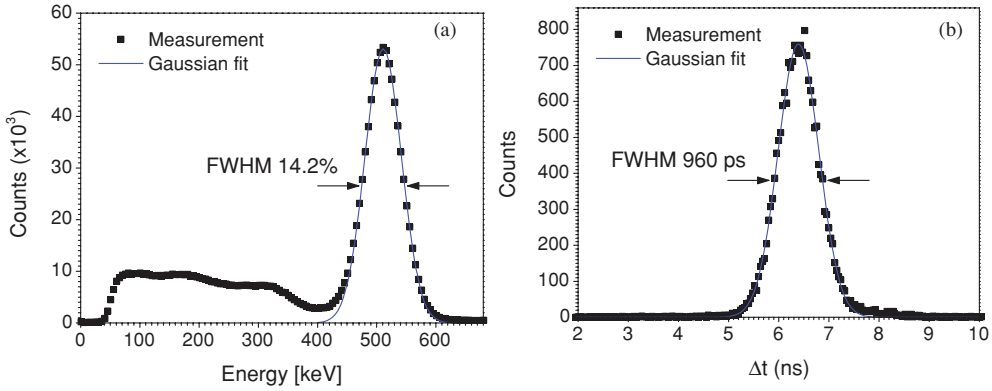


**Figure 7.** Pulse height spectrum (a) measured by irradiating the entire detector with 511 keV photons. Timing spectrum (b) measured in coincidence with a $BaF_2$ detector. Both spectra were measured in FSR geometry. Black squares represent measured data, while solid blue lines indicate Gaussian fits.

### *3.4. Energy and timing resolution*

The black squares in figure 7(a) show a typical pulse height spectrum measured with 511 keV photons. As explained in section 2.3, the entire detector surface was uniformly irradiated. The full-energy peak contains ∼60% of the total number of counts recorded, while the probability of the photoelectric interaction of 511 keV photons in LYSO:$Ce^{3+}$ equals ∼30% of the total probability of interaction. This is attributed to the relatively large size of the crystal: a significant fraction of the detected annihilation photons undergo Compton scattering before being absorbed completely. A Gaussian fit to the full-energy peak is indicated by the solid blue line. The corresponding energy resolution equals 14.2% FWHM at 511 keV.

Figure 7(b) shows the timing spectrum of the detector, measured in coincidence with a $BaF_2$ crystal. The timing resolution equals 960 ps FWHM. As the contribution of the $BaF_2$ crystal is considered negligible, the CRT of two of the SiPM-based detectors in coincidence is expected to be $0.96 \times \sqrt{2} \approx 1.4$ ns FWHM.

## 4. Discussion and conclusion

A novel, SiPM-array-based, high-resolution, monolithic scintillator PET detector with DOI correction has been developed. As the SiPM array is very thin and composed of low-$Z$ materials only, it can be placed on the front surface of the crystal without significantly disturbing the annihilation photon beam. Such FSR geometry appears to provide better performance than conventional BSR, confirming earlier findings obtained with APD-based monolithic PET detectors (Maas *et al* 2006). The superior performance of FSR is attributed to the fact that ∼60% of the annihilation photons are absorbed in the front half of the crystal. Events occurring closer to the SiPM array result in more sharply peaked light distributions that vary more strongly with the position of interaction. Consequently, these events can be positioned more accurately, as has been discussed by van der Laan *et al* (2006). These results illustrate the potential of SiPMs for the development of novel detector designs aiming at, for example, compactness, DOI determination and MR compatibility.

In FSR geometry, spatial resolutions <1.6 mm FWHM were measured at the detector centre in response to an ∼0.54 mm FWHM diameter test beam. Slightly larger FWHM values were found near the detector edges, very similar to what was found in APD-based monolithic detectors by Maas *et al* (2009). Fully characterizing the dependence of the detector spatial response on the position and angle of incidence would allow these effects to be compensated for during iterative image reconstruction, a topic that warrants further research. Hardly any resolution losses were observed at angles of incidence of up to 45°, demonstrating excellent DOI correction. About 14% FWHM energy resolution was obtained. The single detector timing resolution is estimated to be 960 ps FWHM, translating into a CRT of ∼1.4 ns for two detectors in coincidence.

The present results may be compared to those obtained recently by other authors using SiPM arrays. Kolb *et al* (2008) could resolve a 12 × 12 array of 1.5 mm × 1.5 mm × 10 mm LYSO:$Ce^{3+}$ pixels using a 3 × 3 array, made in-house using 3 mm × 3 mm SiPMs and dedicated light guides. They achieved a single detector timing resolution of 950 ps FWHM and ∼22% FWHM energy resolution. España *et al* (2008) nicely resolved a 4 × 4 array of 1.5 mm × 1.5 mm × 12 mm LYSO:$Ce^{3+}$ pixels using a 6 mm × 6 mm active area, monolithic 2 × 2 SiPM array. They obtained energy resolutions between 11% and 22% FWHM for single crystals at different locations on the array, but provided no information on timing resolution yet. Llosá *et al* (2008) reported ∼15% FWHM energy resolution and a CRT of ∼1.4 ns FWHM using 4 mm × 4 mm × 5 mm monolithic LYSO:$Ce^{3+}$ crystals coupled to a SiPM array consisting of 4 × 4 pixels of 1 mm × 1 mm size in a common substrate, in preparation of spatial resolution measurements.

While very similar timing resolutions were obtained with all approaches, the energy resolution tends to be better for monolithic crystals. All detectors appear to achieve good spatial resolution, although it is to be noted that the position information obtained with pixelated crystals is discrete (crystal identification), whereas our approach yields (pseudo-) continuous coordinates. An advantage of monolithic scintillators is that the reduction of inter-crystal dead space results in higher system sensitivity (van der Laan *et al* 2007). Another important advantage of the present approach is the excellent DOI correction.

The spatial resolution obtained in this work is slightly worse than that achieved with APD-based monolithic detectors by Maas *et al* (2009). This is mainly attributed to the relatively low PDE of the active area of the present SiPM arrays, namely ∼6%, compared to 25–30% for PMTs and up to ∼75% for APDs. However, the spatial resolution obtained with APDs is inherently limited by their relatively large excess noise factor and dark current, as analysed quantitatively by Maas *et al* (2008). Due to the relatively low gain of APDs, preamplifier noise is another limiting factor. Thus, further improvement of the SiPM photo-detection efficiency might eventually result in better spatial resolution than can be obtained with APDs.

Although the timing resolution obtained with SiPM arrays is considerably better than that of APD-based monolithic PET detectors (Maas *et al* 2009), it is still insufficient for TOF-PET (Muehllehner and Karp 2006). In fact, obtaining the best possible timing resolution has not been emphasized upon in this work, as the present quality of the SiPM arrays used was not expected to allow CRTs significantly smaller than 1 ns. Nevertheless, CRTs $\leqslant$240 ps have recently been demonstrated with small LYSO:$Ce^{3+}$ and $LaBr_3$:$Ce^{3+}$ crystals coupled to 3 mm × 3 mm SiPMs having higher PDE and lower dark current (Kim *et al* 2008, Schaart *et al* 2008a), demonstrating that TOF determination with SiPM-based scintillation detectors is in principle feasible.

We conclude that SiPMs are a very promising new class of light sensors for use in PET scintillation detectors and that further improvement of these devices may lead to detectors with unsurpassed overall performance.

## Acknowledgments

This work was supported in part by SenterNovem under grant no IS055019. We would like to thank SensL, in particular Deborah Herbert, for providing the SiPM array photograph and for discussions on the PDE of the device.

## References

Antich P P, Tsyganova E N, Malakhovc N A and Sadygovc Z Y 1997 Avalanche photo diode with local negative feedback sensitive to UV, blue and green light *Nucl. Instrum. Methods Phys. Res.* A **389** 491–8

Beyer T *et al* 2000 A combined PET/CT scanner for clinical oncology *J. Nucl. Med.* **41** 1369–79

Bondarenko G *et al* 2000 Limited Geiger-mode microcell silicon photodiode: new results *Nucl. Instrum. Methods Phys. Res.* A **442** 187–92

Britvitch I, Johnson I, Renker D, Stoykov A and Lorenz E 2007 Characterization of Geiger-mode avalanche photodiodes for medical imaging applications *Nucl. Instrum. Methods Phys. Res.* A **571** 308–11

Catana C, Wu Y, Judenhofer M S, Qi J, Pichler B J and Cherry S R 2006 Simultaneous acquisition of multislice PET and MR images: initial results with a MR-compatible PET scanner *J. Nucl. Med.* **47** 1968–76

Cherry S R 2004 *In vivo* molecular and genomic imaging: new challenges for imaging physics *Phys. Med. Biol.* **49** R13–48

Czernin J, Allen-Auerbach M and Schelbert H R 2007 Improvements in cancer staging with PET/CT: literature-based evidence as of September 2006 *J. Nucl. Med.* **48** Suppl 1 78S–88S

de Haas J T M and Dorenbos P 2008 Advances in yield calibration of scintillators *IEEE Trans. Nucl. Sci.* **55** 1086–92

España S, Tapias G, Fraile L M, Herraiz J L, Vicente E, Udias J, Desco M and Vaquero J J 2008 Performance evaluation of SiPM detectors for PET imaging in the presence of magnetic fields *2008 IEEE Nucl. Sci. Symp. Conf. Record* pp 3591–5

Gambhir S S 2002 Molecular imaging of cancer with positron emission tomography *Nat. Rev. Cancer* **2** 683–93

Golovin V and Saveliev V 2004 Novel type of avalanche photodetector with Geiger mode operation *Nucl. Instrum. Methods Phys. Res.* A **518** 560–4

Herbert D J, Moehrs S, D'Ascenzo N, Belcari N, Del Guerra A, Morsani F and Saveliev V 2007 The silicon photomultiplier for application to high-resolution positron emission tomography *Nucl. Instrum. Methods Phys. Res.* A **573** 84–7

Israel O and Kuten A 2007 Early detection of cancer recurrence: $^{18}$F-FDG PET/CT can make a difference in diagnosis and patient care *J. Nucl. Med.* **48** (Suppl. 1) 28S–35S

Jan S *et al* 2004 GATE: a simulation toolkit for PET and SPECT *Phys. Med. Biol.* **49** 4543–61

Judenhofer M S *et al* 2008 Simultaneous PET-MRI: a new approach for functional and morphological imaging *Nat. Med.* **14** 459–65

Kim C L, Wang G C and Dolinsky S 2008 Multi-pixel photon counters for TOF PET detector and its challenges *2008 IEEE Nucl. Sci. Symp. Conf. Record* pp 3586–90

Kolb A, Judenhofer M S, Lorenz E, Renker D and Pichler B J 2008 PET block detector readout approaches using G-APDs *2008 IEEE Nucl. Sci. Symp. Conf. Record*

Lewellen T K 2008 Recent developments in PET detector technology *Phys. Med. Biol.* **53** R287–317

Llosá G *et al* 2008 Evaluation of the first silicon photomultiplier matrices for a small animal PET scanner *2008 IEEE Nucl. Sci. Symp. Conf. Record* pp 3574–80

Maas M C, Schaart D R, Van Der Laan D J, Bruyndonckx P, Lemaître C, Beekman F J and van Eijk C W E 2009 Monolithic scintillator PET detectors with intrinsic depth-of-interaction correction *Phys. Med. Biol.* **54** 1893–908

Maas M C, Schaart D R, Van Der Laan D J, van Dam H T, Huizenga J, Brouwer J C, Bruyndonckx P, Lemaître C and van Eijk C W E 2008 Signal to noise ratio of APD-based monolithic scintillator detectors for high resolution PET *IEEE Trans. Nucl. Sci.* **55** 842–52

Maas M C, Van Der Laan D J, Schaart D R, Huizenga J, Brouwer J C, Bruyndonckx P, Léonard S, Lemaître C and van Eijk C W E 2006 Experimental characterization of monolithic-crystal small animal PET detectors read out by APD arrays *IEEE Trans. Nucl. Sci.* **53** 1071–7

McElroy D P, Saveliev V, Reznik A and Rowlands L A 2007 Evaluation of silicon photomultipliers: a promising new detector for MR compatible PET *Nucl. Instrum. Methods Phys. Res.* A **571** 106–9

Moses W W 2007 Recent advances and future advances in time-of-flight PET *Nucl. Instrum. Methods Phys. Res.* A **580** 919–24

Muehllehner G and Karp J S 2006 Positron emission tomography *Phys. Med. Biol.* **51** R117–37

Musienko Y, Auffray E, Lecoq P, Reucroft S, Swain J and Trummer J 2007 Study of multi-pixel Geiger-mode avalanche photodiodes as a read-out for PET *Nucl. Instrum. Methods Phys. Res.* A **571** 362–5

Nestle U, Weber W, Hentschel M and Grosu A-L 2009 Biological imaging in radiation therapy: role of PET *Phys. Med. Biol.* **54** R1–25

Phelps M E 2000 Positron emission tomography provides molecular imaging of biological processes *Proc. Natl Acad. Sci. USA* **97** 9226–33

Renker D 2007 New trends in photodetectors *Nucl. Instrum. Methods Phys. Res.* A **71** 1–6

Rohren E M, Turkington T G and Coleman E 2004 Clinical applications of PET in oncology *Radiology* **231** 305–32

Schaart D R, Seifert S, van Dam H T, de Boer M R, Vinke R, Dendooven P, Löhner H and Beekman F J 2008a First experiments with $LaBr_3$:Ce crystals coupled directly to silicon photomultipliers for PET applications *2008 IEEE Nucl. Sci. Symp. Conf. Record* pp 3991–4

Schaart D R, van Dam H T, Seifert S, Vinke R, Dendooven P, Löhner H and Beekman F J 2008b SiPM-array based PET detectors with depth-of-interaction correction *2008 IEEE Nucl. Sci. Symp. Conf. Record* pp 3581–5

Seifert S, Schaart D R, van Dam H T, Huizenga J, Vinke R, Dendooven P, Löhner H and Beekman F J 2008 A high bandwidth preamplifier for SiPM-based TOF PET scintillation detectors *2008 IEEE Nucl. Sci. Symp. Conf. Record* pp 1616–9

SensL 2007 SPM photon detection efficiency Rev 1.4, December 2007 *SensL Technical Note* http://www.sensl.com/pdfs/SPM_Tech_App_Notes/TN_PDE.pdf

Shao Y, Cherry S R, Farahani K, Slates R, Silverman R W, Meadors K, Bowery A, Siegel S, Marsden P K and Garlick P B 1997 Development of a PET detector system compatible with MRI/NMR systems *IEEE Trans. Nucl. Sci.* **44** 1167–71

Surti S, Kuhn A, Werner M E, Perkins A E, Kolthammer J and Karp J S 2007 Performance of Philips Gemini TF PET/CT scanner with special consideration for its time-of-flight imaging capabilities *J. Nucl. Med.* **48** 471–80

Townsend D W 2008 Multimodality imaging of structure and function *Phys. Med. Biol.* **53** R1–39

Van Der Laan D J, Maas M C, de Jong H W A M, Schaart D R, Bruyndonckx P, Lemaître C and van Eijk C W E 2007 Simulated performance of a small-animal PET scanner based on monolithic scintillation detectors *Nucl. Instrum. Methods Phys. Res.* A **571** 227–30

Van Der Laan D J, Maas M C, Schaart D R, Bruyndonckx P, Léonard S and van Eijk C W E 2006 Using Cramér-Rao theory combined with Monte Carlo simulations for the optimization of monolithic scintillator PET detectors *IEEE Trans. Nucl. Sci.* **53** 1063–70